# Microstructure-Based Random FEM Simulation of Frost Heave: Theory and Implementation

Shaoyang Dong
Graduate Research Assistant
Department of Civil Engineering
Case Western Reserve University
Phone: (216) 280-0667, Email: shaoyang.dong@case.edu

Xiong (Bill) Yu, Ph.D., P. E.
Professor
Department of Civil Engineering
Case Western Reserve University
Phone: (216) 501-2155, Email: xiong.yu@case.edu

Paper Submitted to the Transportation Research Board for Presentation and Publication at the 2018 Annual Meeting in Washington, D. C.

Words: 4920 Tables: 1 Figures: 10 Total: 7420

**ABSTRACT**

Frost heave can cause serious damage to civil infrastructure. For example, interactions of soil and water pipe under frozen conditions have been found to significantly accelerate the pipe fracture. Frost heave may cause the retaining wall along highway to crack even failure in cold climates. This paper describes a holistic model to simulate the temperature, stress and deformation in frozen soil and implement the model to simulate the frost heave and stress in water pipelines. The frozen soil behaviors are based on a microstructure-based random finite element model, which holistically describes the mechanical behaviors of soils subjected to freezing conditions. The new model is able to simulate the bulk behaviors by considering the microstructure of soils. The soil is phase coded and therefore the simulation model only need the corresponding parameters of individual phase. This significantly simplified the needs to obtain parameters needed for the model. The capability of the model in simulating the temperature distribution and volume change are firstly validated with laboratory scale experiments. Coupled thermal-mechanical processes are introduced to describe the soil responses subjected to sub-zero temperature on the ground surface. This subsequently changes the interaction modes between ground and water pipe and leads to increase of stresses in the water pipe. The effects of cracks along the water pipe further cause stress concentration, which jeopardizes the pipe performance and leads to failure. The combined effects of freezing ground and traffic load are further evaluated with the model.

## INTRODUCTION

Frost heave is a phenomenon that soil swells upwards during freezing conditions. It mostly happens in areas of freezing climates limited to frost susceptible soils such as silty soils or clayey soils (*1-2*). Frost heave in cold regions may cause pavement upheaving and cracking, retaining wall and pipeline failures and other serious damage to transportation infrastructure (*3-6*). Previous theories to addressing the frost heave mainly include the Segragation Potential theory (*4*) and the Discrete Icelens theory (*7*). Both theories can be applied to numerical models to predict the frost heave. Frost heave of soils is a complex process which involves thermal flow, hydraulic conduction and stress evolution. It is a coupled multi-physical process which is referred to as the thermal-hydro-mechanical (THM) process (*8-13*). The THM process is coupled by extension of isothermal theory that incorporates the thermal expansion of solid skeleton as well as the pore fluid (*14-15*). Kurashige solved the problem of thermally induced stresses in a poroelastic cylinder by employing the Crank-Nicholson implicit scheme (*16*). The THM process creates a coupling effect that is critical to the behaviors of frozen soils. During the freezing process, the THM coupling effect can lead to decreased water content, increased matric suction, the rise of water pressure head, and the generation of internal stress. A number of researchers have applied the THM coupled finite element analysis to soil. For example, Nishimura developed a coupled-THM model for frozen soil to study the foundation stability, frost heave, and mass movements in cold regions (17). The development of the coupled THM model to simulate frozen soil requires a sound foundation of theoretical mechanisms, accurate parameters obtained from experimental measurements, and reliable numerical methods to implement in the computational simulations.

The thermal, hydraulic, and mechanical properties of soil are quite sensitive to design parameters. Some of the parameters are randomly distributed throughout the soil sample due to complex geological processes. This random process can be simulated by the random-finite element method (RFEM) (*18-20*). These properties may include parameters such as Young's modulus, Poisson's ratio, density, thermal conductivity, heat capacity, coefficiant of thermal expansion and a variety of other parameters (*21-23*). The RFEM is an extension of the traditional FEM that adds randomness to material properties. Fenton combined random field simulation with the non-linear finite element to investigate the active earth pressure and stability of the retaining wall (*24*).

In the microstructural view, frozen soil is a four-phase material that includes soil particles, ice, water, and air, arranged randomly due to complex geological processes (*25*). Researchers have built a microstructural model for soil (*26-27*). Helliwell and Tracy obtained the structure of soil by using X-ray Computed Tomography (CT) images (*28-29*). The microstructure extracted from the high-resolution images provides a foundation for simulating the physical coupling process, which could improve the understanding of THM coupled physics at a multiscale, i.e. micro-scale or pore-scale of soil samples.

This paper describes the development and implementation of random finite element model for the multiphysics thermo-hydro-mechanical processes in frozen soils. The spatial randomness of soil parameters is described with this model. The results unveil interesting phenemena associated with freezing/thawing due to the soil microstructure.

## THEORETICAL BASIS

The theoretical basis for the thermo-hydro-mechanical processes has been established in past years. Three types of physical fields (thermal field, hydraulic field, and mechanical field) fall into the problems of continuum mechanics and the governing equations of these physical fields abide by the laws of energy conservation and mass conservation. The governing equation for the thermal fields (Equation 1) contains the convection and conduction terms, and is modified from Fourier's equation.

$$\rho_j C_{p_j} \frac{\partial T}{\partial t} + \rho_j C_{p_j} q \cdot \nabla T = \nabla \cdot (k_j \nabla T) \tag{1}$$

Where the subscript $j$ denotes different phases of the poromaterial; $\rho_j$ is the density; $C_{pj}$ is the heat capacity; $k_j$ is the thermal conductivity; $T$ is the temperature; $t$ is time and $q$ is the flux.

The flow of moisture is described with the Darcy's law (Equation 2):

$$q = -\frac{\kappa_j}{\mu} \nabla p \tag{2}$$

Where $p$ is the pore-water pressure; $\kappa_j$ is the intrinsic permeability; $\mu$ is the dynamic viscosity and $q$ is the flux.

The governing equation for the mechanical field is the Navier's equation, which includes strain-displacement correlation (Equation 3), the constitutive relationship (Equation 4) and the equation of motion (Equation 5).

The strain-displacement correlation is

$$\varepsilon_j = \frac{1}{2}[\nabla \mathrm{u}_j + (\nabla \mathrm{u}_j)^T] \tag{3}$$

Where $\varepsilon_j$ is the strain tensor; $u_j$ is the displacement vector.

The constitutive relationship for phase j of the porous material is

$$\sigma_j = \mathrm{D}_j(\varepsilon - \varepsilon_0 - \varepsilon_{th_j} - \varepsilon_{tr} - \varepsilon_{hp}) + \sigma_{0,j} \tag{4}$$

Where $Dj$ is the stiffness matrix of phase j; $\sigma$ is the stress tensor; $\sigma_0$ is the initial stress tensor; $\varepsilon$ is the total strain tensor; $\varepsilon_0$ is the initial strain; $\varepsilon_{thj}$ is the strain caused by thermal expansion of phase j; $\varepsilon_{tr}$ is the strain resulting from the phase change of water, which is $0.09Q$, where $Q$ is the amount of water that changes into ice and 0.09 is the relative change of volume when water changes into ice; $\varepsilon_{hp}$ is the strain caused by the change of matric suction, which is calculated by $h/H$, where $h$ is the water head and $H$ is the modulus related to the matric suction.

The equation of motion is

$$\nabla \cdot (\mathrm{C}_j \nabla \mathrm{u}_j) + \mathrm{F} = \rho_j \ddot{\mathrm{u}}_j \tag{5}$$

Where $C_j$ is the stiffness tensor of the material; $u_j$ is the displacement vector; $\rho_j$ is the density, and F is the body force.

## EXPERIMENTAL MEASUREMENTS OF FROZEN SOIL

Two identical cylindered silt specimens of 3.3 cm in diameter and 7.2 cm in height were prepared with Harvard miniature compactor. The specimens have saturated gravimetric water content of 22%. The dry density of the silt specimen is 1.708 g/cm$^3$ and the initial temperature is 20 degrees Celsius. The specimens were thermally insulated on sides and at the bottom to create one dimensional thermal flow. The wrapped specimens were placed in the freezer with a temperature of -20 degrees Celsius. Thermal couples were installed in the silt specimen at the location of 10 mm, 30 mm and 50 mm from top of the specimen to measure the temperature distribution of the silt specimens during the freezing process. Two different methods are utilized to measure the vertical deformations of the specimens during the freezing process, which include manual measurement with dial gauge indicator and automatic measurement with a laser displacement transducer (Figure 1). The performance of these methods are compared from the measurement on two separate specimens.

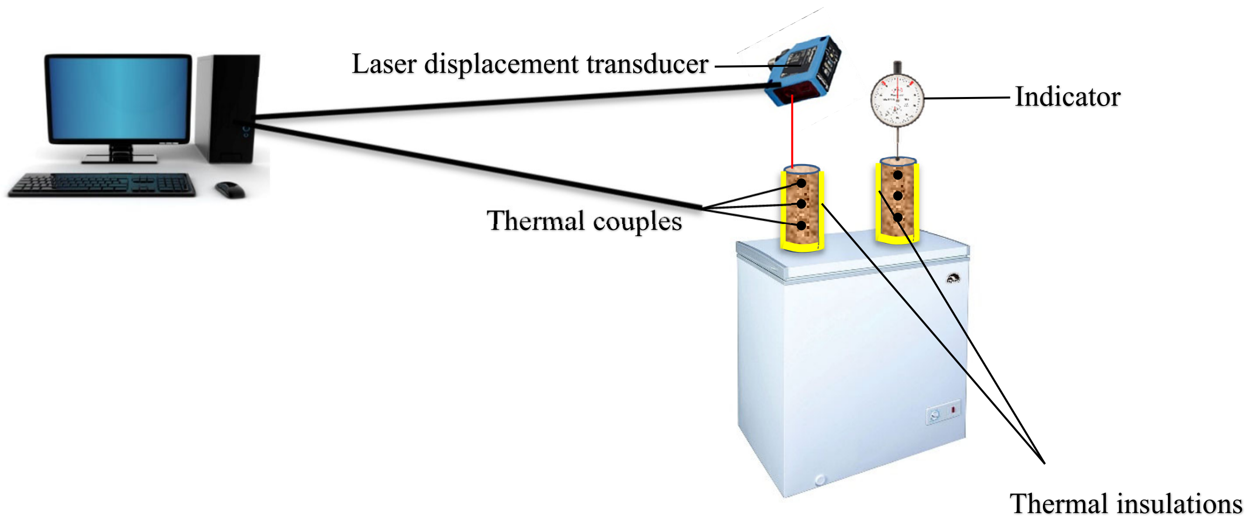


**FIGURE 1 The schematic picture of the experimental system measuring the frozen soil**

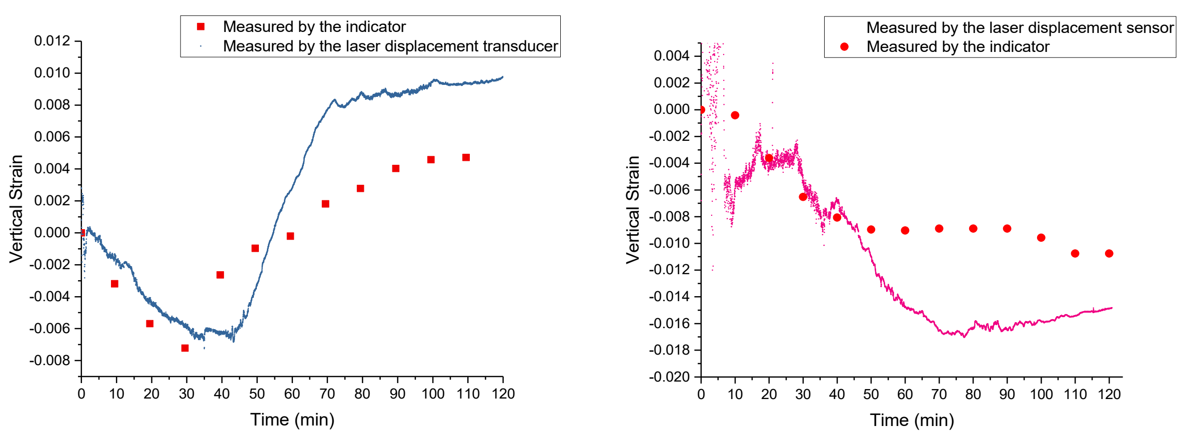


Freezing Thawing

**FIGURE 2 The vertical strains of the saturated silt specimen during the freezing and thawing processes**

The laser displacement transducer and the thermal couples were connected to the computer to monitor and record the vertical deformation and temperature distribution of the silt specimens during the freezing process. The vertical strains and the temperature distribution of the silt specimen during the freezing process are plotted in Figure 2 and Figure 3, respectively.

For the silt specimen measured by the indicator, the vertical strain decreased from 0 to -0.007 in the first half hour due to the compaction of matric suction, then the vertical strain of the specimen increased from -0.007 to 0.005 for the rest of the time due to the frost heave. For the silt specimen measured by the laser displacement transducer, the vertical strain decreased from 0 to -0.0065 in the first 35 minutes due to the compaction of matric suction, then the vertical strain of the specimen increased from -0.0065 to 0.01 for the rest of the time due to the frost heave. From Figure 2, it is observed that the vertical strain measured by the indicator is smaller than that measured by the laser displacement transducer because the silt specimen was pressed by the indicator so that the vertical deformation was reduced; while the vertical strain measured by the laser was non-contact measurement. It is also observed that the vertical strain measured by the indicator reached to the lowest value 5 minutes earlier than that measured by the laser displacement transducer. It is due to contact between the metal stick of the indicator and the silt specimen, the measuring point on the silt specimen froze faster and arrived at the frozen proint earlier. So it can be concluded that during the freezing process, the vertical strain measured by the indicator is less reliable than that measured by the laser displacment transducer.

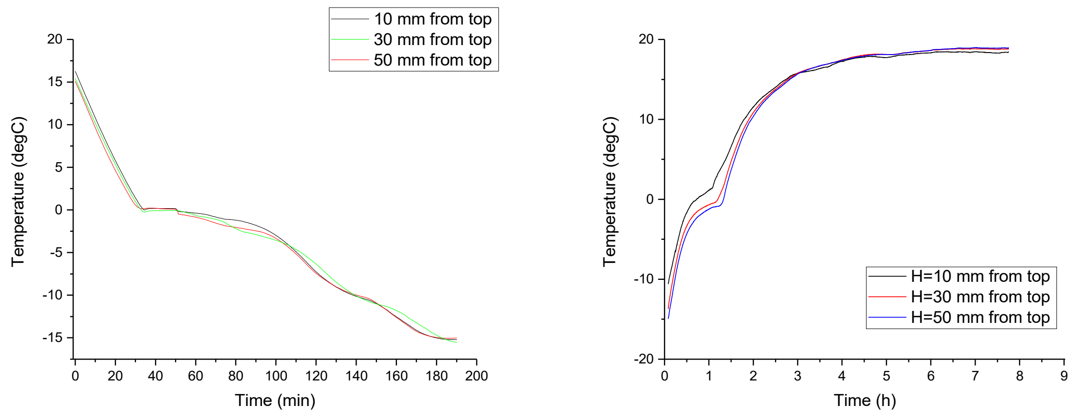


Freezing Thawing

**FIGURE 3 The temperature of the saturated silt specimen during the freezing and thawing processes**

As shown in Figure 3, the temperature decreased fast above 0 degrees Celsius, and then it decreased at a slower rate at around 0 degrees Celsius due to the latent heat of fusion. The temperature decreased fast again below the 0 degrees Celsius and gradually approach to the temperature in the freezer. Comparing Figure 3 and Figure 2 we can find that during the phase change period (35 min to 80 min), the vertical strain of the silt specimen sharply increased due to the expansion of the ice phase.

The frozen silt specimens with thermal couples were taken out from the freezer to the laboratory with a temperature of 19 degrees Celsius, at the same time, the thermal couples were connected to the computer to monitor and record the temperature during the thawing process. The laser displacement transducer and indicator were also applied to measure the vertical deformation of the silt specimens. The vertical strains and the temperature distribution of the silt specimen during the thawing process are plotted in Figure 2 and Figure 3, respectively.

For the silt specimen measured by the indicator, the vertical strain decreased from 0 to -0.009 in the first 50 min, then, the vertical strain came to a stable level during 50 min to 90 min because the matric potential decreased which caused volume expansion counteracting the decreases in the volume due to phase change of ice. The vertical deformation continued to decrease and gradually became stable to be -0.01 for the rest of the time. For the silt specimen measured by the laser displacement sensor, the measured data were not stable in the first half hour. It was observed that the ice crystal on top of the silt specimen melted into water in the first half hour. It is speculated that the ice crystal melting accouts for the unstable measurement of the verticle strain. The vertical strain decreased during 30 min to 80 min of thawing due to phase change of ice. The vertical deformation became stable to be -0.015 for the rest of the time. The absolute value of vertical strain measured by the indicator is smaller than that measured by the laser displacement transdusor.

As shown in Figure 3, the temperature increased fast below 0 degrees Celsius, and then it increased slowly around 0 degrees Celsius due to the latent heat of fusion. The temperature grew fast again above 0 degrees Celsius and gradually approached to the environment temperature. It took about six hours for the silt specimen to reach a thermal balance condition (the temperature of the silt specimen is the same to the environment). Since the thermal flow travelled from top of the silt specimen to the bottom, the temperature at the higher location is larger than that of the lower location on the silt specimen at a given time.

## NUMERICAL SIMULATION OF FROZEN SOIL

The physical properties of a silt specimen prepared by harvard miniature compactor was measured experimentally in the previous part. To simulate the microstructure of frozen soils, firstly, the volumetric content of each phase is calculated from its dry density (1.708 g/cm$^3$), initial gravimetric water content (22%), and specific gravity (2.65) of the silt specimen. The next step is to generate an m×n matrix in Matlab. In the matrix, m is equal to the height of the silt specimen divided by the diameter of the silt particle, while n is equal to the radius of the silt specimen divided by the diameter of the silt particle. Thus, m×n equals the total number of elements in the image of 2-D silt model. Each element in the matrix represents a particular phase of the silt specimen, and different numbers (0, 1/3, 2/3, 1) are assigned to the elements in the matrix to represent four different phases within the silt specimen. These numbers are randomly assigned, and their probability of occurrence is equal to the volumetric content of each phase. The final step is to generate an image from the matrix in Matlab. Each pixel of the image represents each element in the matrix, and the color in the pixel corresponds to the number in the element. Four different colors (black, dark grey, light grey, and white) represent the soil particles, ice, water and air, respectively (Figure 4). The probability of occurrence of each color equals the volumetric content of each phase.

The microstructure image is imported to COMSOL and material properties are assigned based on the color scale of the image. Four different colors (dark blue, light blue, yellow, and red) represent the soil particles, ice, water and air, respectively (Figure 4). Figure 4 shows the 2-D silt images at different degrees of thawing after conversion from Matlab to Comsol model.

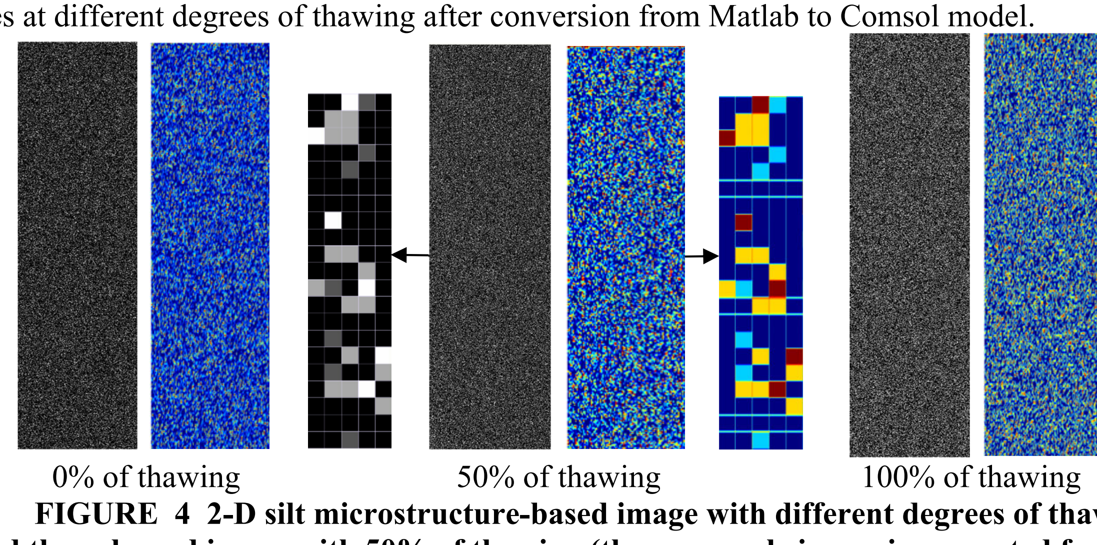

0% of thawing 50% of thawing 100% of thawing

**FIGURE 4 2-D silt microstructure-based image with different degrees of thawing and the enlarged image with 50% of thawing (the gray-scale image is generated from Matlab, the color image is converted into Comsol)**

With the microstructure based random FEM model, the thermal parameters can be assigned to each pixel based on the color of the image, which represents individual phase. The heat capacity, thermal conductivity, and density of the air, water, ice, and silt particles are assigned to each pixel based on different colors corresponding to different phases in the silt specimen. The thermal parameter values of each phase are listed in Table 1.

**Table 1 Constant parameters for the simulation**

| Constant | Value | Units | Description |
|---|---|---|---|
| $R$ | 1.65 | cm | Radius of silt specimen |
| $H$ | 7.2 | cm | Height of silt specimen |
| $w_0$ | 0.22 | 1 | Initial water content |
| $\rho$ | 1708 | kg/m$^3$ | Dry density of silt specimen |
| $d$ | 150 | μm | Diameter of silt particle |
| $G_s$ | 2.65 | 1 | Specific gravity of silt specimen |
| $E_s$ | 12.7 | GPa | Young's modulus of silt particle |
| $E_i$ | 9 | GPa | Young's modulus of ice |
| $E_w$ | $3.9\times10^{-5}$ | Pa | Young's modulus of water |
| $E_a$ | 0 | Pa | Young's modulus of air |
| $E_p$ | 205 | GPa | Young's modulus of the steel pipeline |
| $\mu_s$ | 0.3 | 1 | Poisson's ratio of silt particle |
| $\mu_i$ | 0.3 | 1 | Poisson's ratio of ice |
| $\mu_w$ | 0.5 | 1 | Poisson's ratio of water |
| $\mu_a$ | 0 | 1 | Poisson's ratio of air |
| $\mu_p$ | 0.28 | 1 | Poisson's ratio of the steel pipeline |
| $\rho_s$ | 2600 | kg/m$^3$ | Density of silt particle |
| $\rho_i$ | 917 | kg/m$^3$ | Density of ice |
| $\rho_w$ | 1000 | kg/m$^3$ | Density of water |
| $\rho_a$ | 1.29 | kg/m$^3$ | Density of air |
| $\rho_p$ | 7850 | kg/m$^3$ | Density of the steel pipeline |
| $\kappa_s$ | $10^{-17}$ | mm$^2$ | Intrinsic permeability of silt particle |
| $\kappa_i$ | $10^{-17}$ | mm$^2$ | Intrinsic permeability of ice |
| $\kappa_w$ | $3.08\times10^{-13}$ | mm$^2$ | Intrinsic permeability of water |
| $\kappa_a$ | $1.31\times10^{-19}$ | mm$^2$ | Intrinsic permeability of air |
| $\varepsilon$ | 0.3663 | 1 | Porosity of silt specimen |
| $\chi_f$ | $4.6\times10^{-10}$ | 1/Pa | Compressibility of water |
| $\mu$ | $8.9\times10^{-4}$ | Pa·s | Dynamic viscosity of water |
| $k_s$ | 2 | W/m·K | Thermal conductivity of silt particle |
| $k_i$ | 2.2 | W/m·K | Thermal conductivity of ice |
| $k_w$ | 0.58 | W/m·K | Thermal conductivity of water |
| $k_a$ | 0.025 | W/m·K | Thermal conductivity of air |
| $k_p$ | 44.5 | W/m·K | Thermal conductivity of the steel pipeline |
| $Cp_s$ | 835 | J/kg·K | Heat capacity of silt particle |
| $Cp_i$ | 1960 | J/kg·K | Heat capacity of ice |
| $Cp_w$ | 4181.3 | J/kg·K | Heat capacity of water |
| $Cp_a$ | 1005 | J/kg·K | Heat capacity of air |

| | | | |
|---|---|---|---|
| $Cp_p$ | 475 | J/kg·K | Heat capacity of the steel pipeline |
| $L_f$ | 334 | kJ/kg | Latent heat fusion of water |
| $\alpha_s$ | $9\times10^{-6}$ | 1/K | Volumetric coefficient of thermal expansion of silt particle |
| $\alpha_i$ | $1.9\times10^{-4}$ | 1/K | Volumetric coefficient of thermal expansion of ice |
| $\alpha_{i\text{-}w}$ | -0.05 | 1/K | Volumetric coefficient of thermal expansion of a mixture of ice-water |
| $\alpha_w$ | $2.07\times10^{-4}$ | 1/K | Volumetric coefficient of thermal expansion of water |
| $\alpha_a$ | $3.43\times10^{-7}$ | 1/K | Volumetric coefficient of thermal expansion of air |
| $\alpha_p$ | $1.23\times10^{-5}$ | 1/K | Volumetric coefficient of thermal expansion of the steel pipeline |

To simulate the temperature distribution during the thawing process, thermal insulations are applied on sides and the bottom of the 2-D frozen silt model. The initial temperature of the silt specimen is set to -20 degrees Celsius. The boundary temperature is 19 degrees Celsius applied on top of the model during the thawing process.

The calculation procedure of the thermal flow simulation is shown in Figure 5. LiveLink for Comsol is used to link MATLAB process with COMSOL simulation. As indicated in the flow chart, phase changes from ice to water when temperature rises from below zero degrees Celsius to above zero degrees Celsius. The thermal parameters are not only a function of spatially distributed position, but also a function of temperature. By setting the thermal parameters as a step function of temperature and introducing the latent heat fusion of water, it considers the latent heat during phase transition, the simulation is closer to the reality during the phase transition.

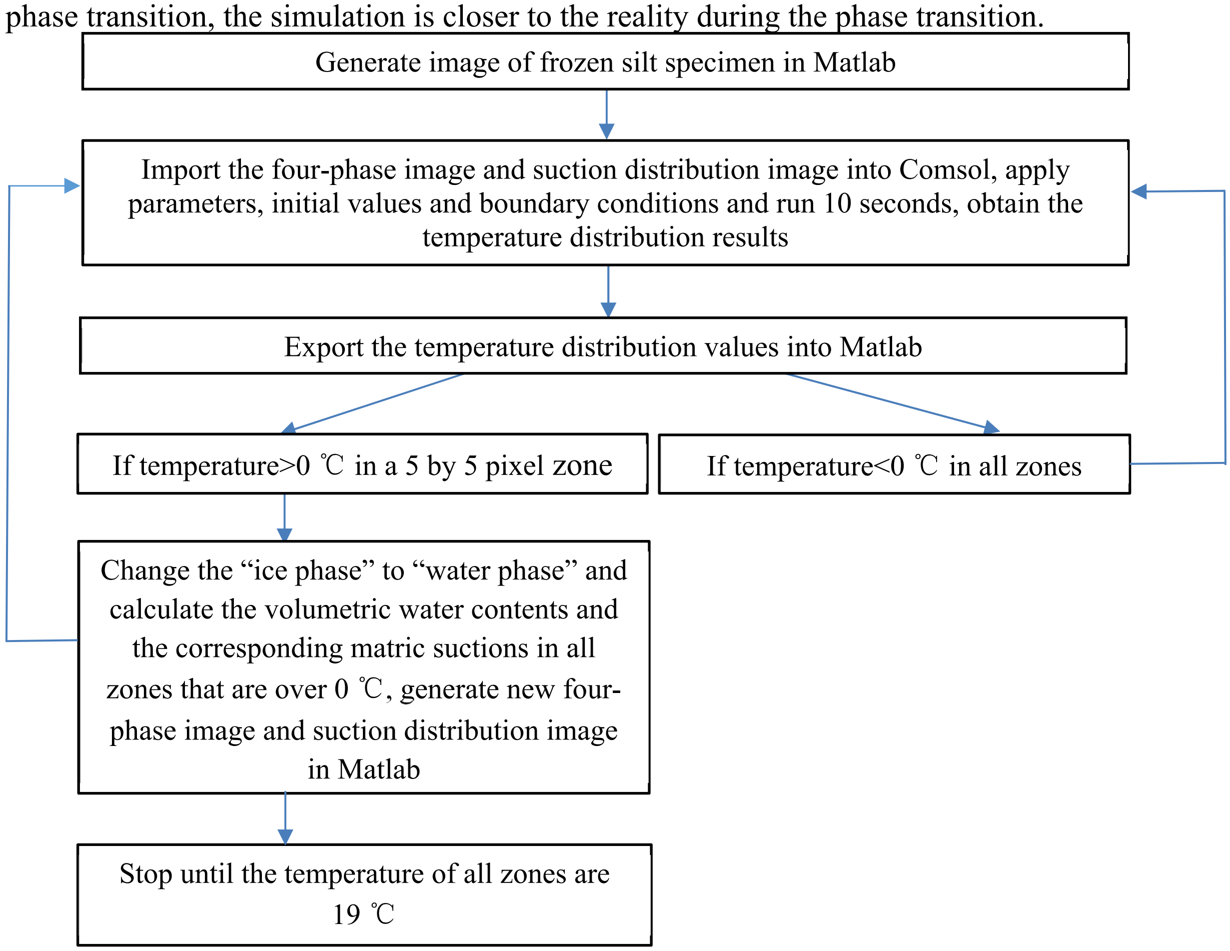

**FIGURE 5 Flow chart of the calculation process of the thermal flow simulation**

Figure 6 compares the numerical simulation and the experimental measurement at different heights of the silt specimen during the thawing process. It takes about 6 hours for the silt to reach a thermal balance condition of similar temperature across the specimen. The numerical simulaion agrees quite well with the experimental measurement, which validates the reliability of this newly developed microstructure based ramdom finite element model.

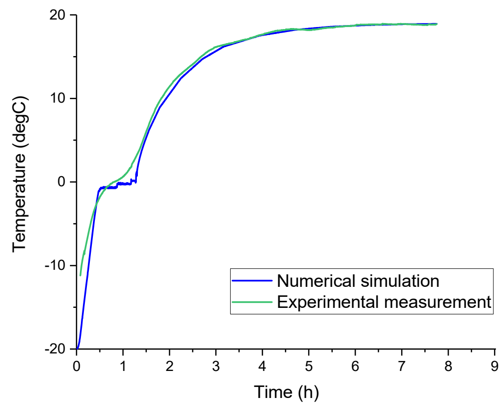


H=10 mm from top

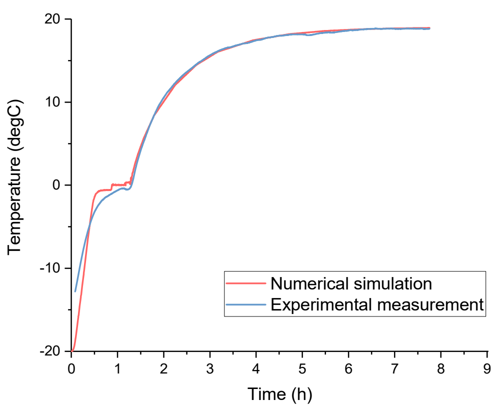


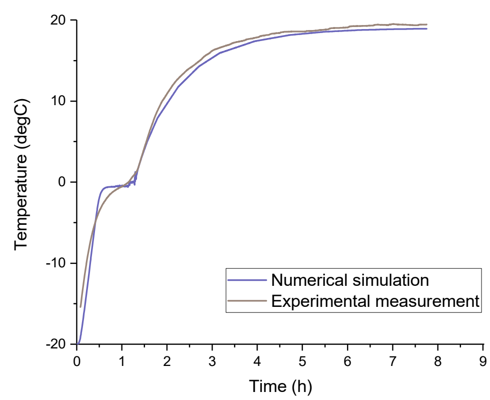


H=30 mm from top

H=50 mm from top

**FIGURE 6 Comparison of the numerical simulation and the experimental measurement at different heights of the silt specimen during the thawing process**

The mechanical parameters can also be assigned to each phase based on the microstructure of random FEM. The Young's modulus, Poisson's ratio, density, and volumetric coefficient of thermal expansion of the air, water, ice, and silt particles (Table 1) are assigned to each pixel based on different colors corresponding to different phases in the silt specimen. The thermal properties of water are modelled with a non-constant value to account for the volume change during phase transition (9% of volume expansion when water freeze into ice).

To demonstrate the production of internal stress and vertical strain during the freezing process, a simulation case is designed in Comsol where thermal insulations are applied on the sides and the bottom of the 2-D unfrozen silt model. The initial temperature of the silt specimen is set to 20 degrees Celsius. The boundary temperature of -20 degrees Celsius is applied on top surface of the model to start the freezing process. The Heat transfer module, the Solid mechanics module and the Poroelasticity module are applied to simulate the temperature distribution and frost heave in the soil specimen. The internal stress is generated by the development of matric suction and thermal expansion due to phase transition. Figure 7 shows the development of internal stress distribution of silt specimen during the freezing process. As the freezing process starts, there is continuous increases in the internal stress. Overall, the model describes the mechanism of internal stress generation based on physical mechanism.

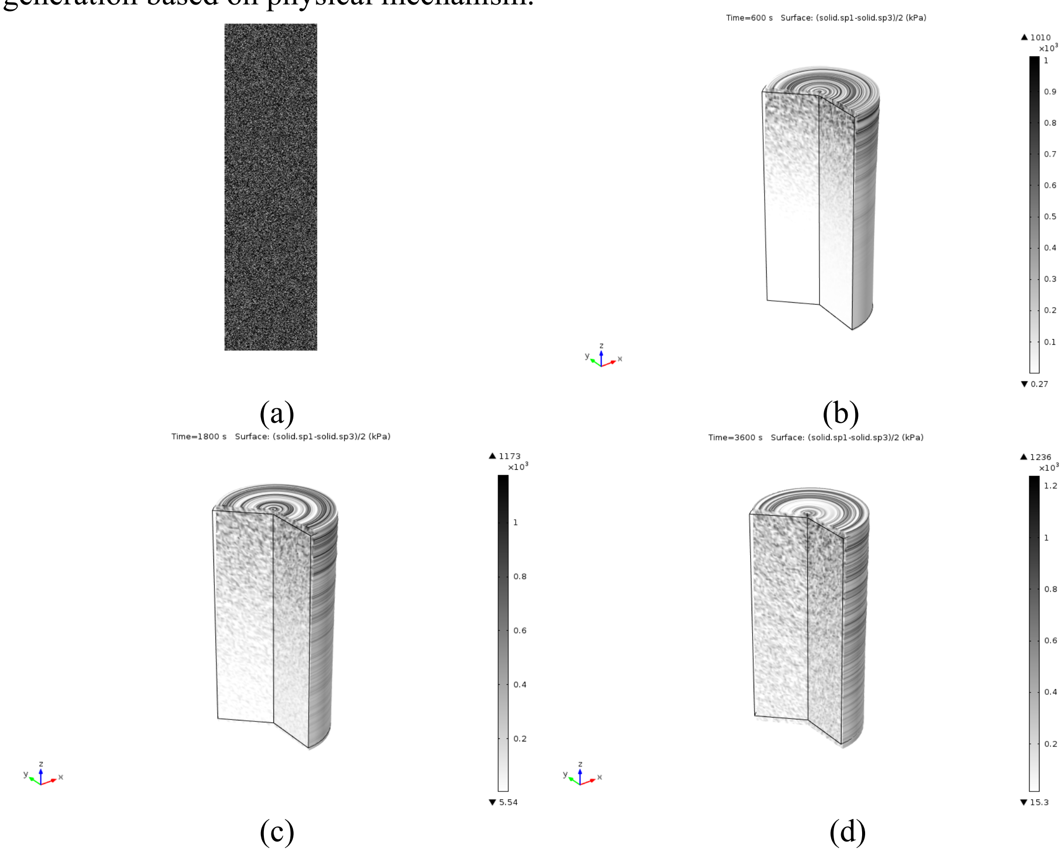


**FIGURE 7 The internal shear stress (Pa) distribution of 3-D silt specimen during the freezing process. (a) The microstructure-based image indicating the initial conditions before freezing (b) after 10 minute; (c) after 30 minutes; (d) after one hour**

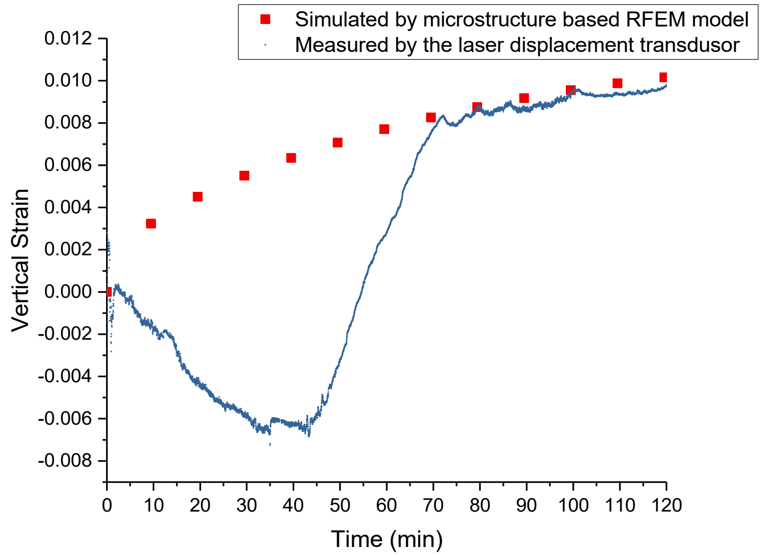


**FIGURE 8 Comparison of the vertical strains of the silt specimen between experimental measurement and numerical simulation during the freezing process**

Figure 8 plots the maximum vertical strain simulated by the microstructure based RFEM and compared the results with experimental data. Overall the volume expansion at the end of freezing process predicted by the RFEM is close to the data measured by the laser displacement transducer. Compared with the experimental data, the simulation results does not show an initial decreases in the soil volume due to increases in the matrix suction. This is possibly as the RFEM model has not considered the effects of matric suction plus the variation of the stiffness of frozen soil with different extent of freezing is not accurately accounted for. This is an aspect in the RFEM model that will be further refined in the further work. Overall, the results of simulating experimental freezing/thawing process indicate that the RFEM model is able to accurately describe the internal stress and volume change due to phase transition associated with freezing.

## SIMULATION CASE STUDY

A water pipeline is buried 1.2m deep in a 30m×5m silt layer. The pipeline has a radius of 0.5m and thickness of 0.02m (Figure 9). The simulation parameters of the silt layer and the pipeline are shown in Table 1.

Thermal insulations are applied on sides and the bottom of the 2-D study region. The initial temperature of the study region is set to 5 degrees Celsius. The boundary temperature is -20 degrees Celsius applied on top of the region during the freezing process. Fixed constraint is applied at the bottom of the study region and rollers are applied on sides of the study region.

After 30 days of freezing, the stress distribution in the intact pipeline, in the defective pipeline, in the pipeline with a point load of 15kN and 480kN exerted on the silt layer surface above the pipeline are shown in Figure 9.

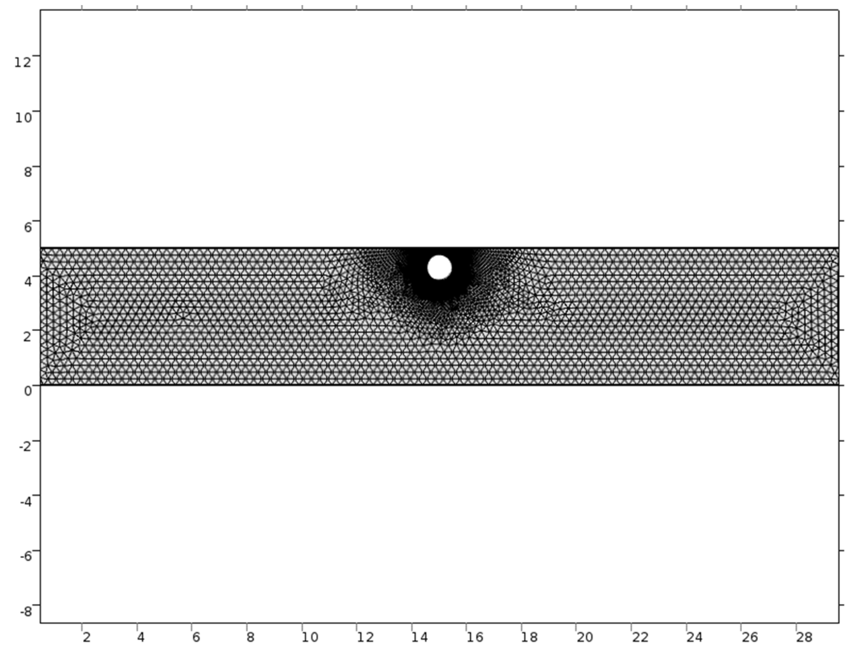

Figure 9 Simulation domain and mesh

As shown in Figure 10, after 30 days of freezing, frost heave leads to increase of stresses in the water pipe. The crack in the water pipe further leads to stress concentration, and increases the maximum stress in the water pipe. The defective pipeline with loads on the surface accelerates the internal stress generation, causes deformation and even failure of the water pipeline.

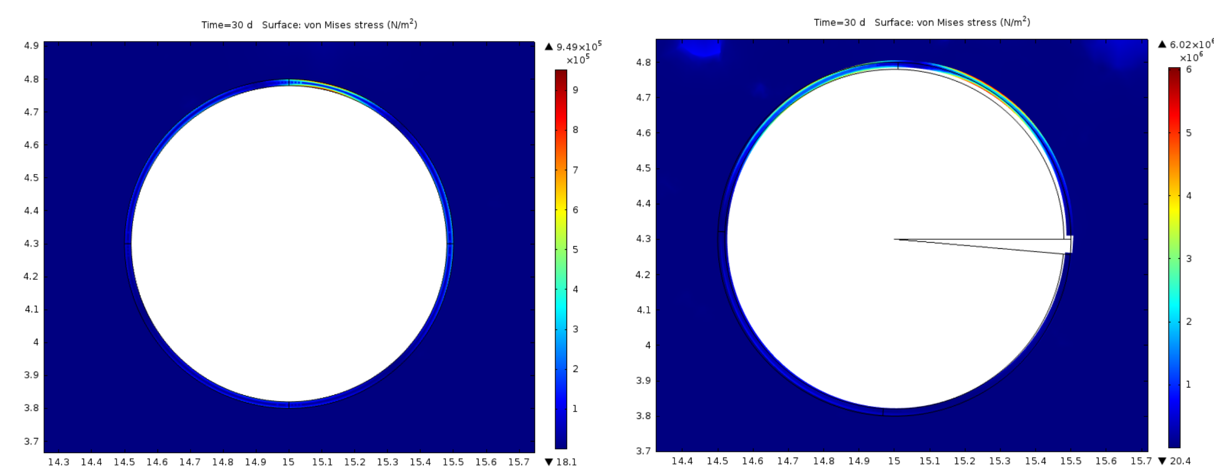


The intact pipeline The defective pipeline

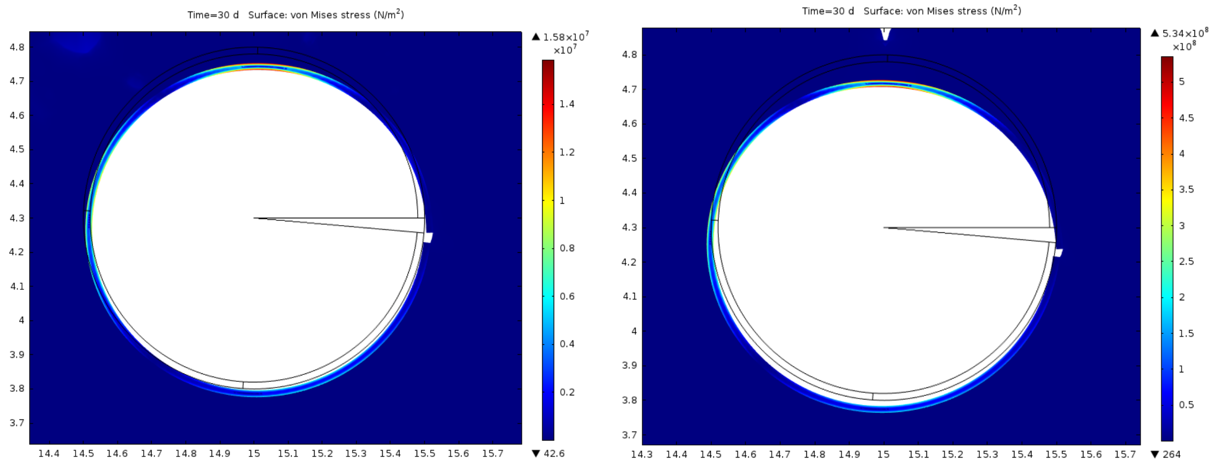


Point load of 15kN on surface　　　Point load of 480kN on surface

**FIGURE 10 Stress distribution in the water pipeline buried in a saturated silt layer after 30 days of freezing**

## CONCLUSION

This research develops a microstructure-based random finite element simulation model to simulate frost heave in saturated soils. This model is able to simulate the bulk behaviors by considering the microstructures. The soil is phase coded and therefore only need the parameters of individual phase. This therefore can direct the efforts to understand the behaviors of individual phase, which represent a more uniform material. The results are consistent with experimental observations. The model holistically accounts for volume change during water phase transition and simulate the production of internal stress due to such process. The modeling approach combines the advantages of discrete element model in simulating the mechanical behaviors of particulate system and the computational efficiency of finite element model. With experimental validation, it provides a new and reliable simulation tool to predict frost induced stress on infrastructures (such as pipelines, retaining walls, etc.). The insight will help guide the engineering design in cold regions.

## ACKNOWLEDGMENTS

This research is partially supported by the Ohio Department of Transportation and US National Science Foundation.

## REFERENCE

1. O'Neill, K., and Miller, R. D. Exploration of a Rigid Ice Model of Frost Heave. *Water Resources Research*, 1985, 21(3), pp. 281-296.
2. Chamberlain, E. J. A Freeze-Thaw Test to Determine the Frost Susceptibility of Soils, Special Report 87-1, U. S. Army Corps of Engineers, Cold Regions Research and Engineering Laboratory, 1987.
3. Nixon, J. F., Morgenstern, N. R., and Reesor, S. N. Frost Heave-Pipeline Interaction Using Continuum Mechanics. *Canadian Geotechnical Journal*, 1983, 20(2), pp. 251-261.
4. Konrad, J. M., and Morgenstern, N. R. Frost Heave Prediction of Chilled Pipelines Buried in Unfrozen Soils. *Canadian Geotechnical Journal*, 1984, 21(1), pp. 100-115.

5. Lai, Y., Wu, Z., Liu, S., and Den, X. Nonlinear Analyses for the Semicoupled Problem of Temperature, Seepage, and Stress fields in Cold Region Retaining Walls. *Journal of thermal stresses*, 2001, 24(12), pp. 1199-1216.
6. Wu., Q., Liu., Y., Zhang., J., and Tong C. A Review of Recent Frozen Soil Engineering in Permafrost Regions along Qinghai-Tibet Highway, China. *Permafrost and Periglacial Processes*, 2002, 13, pp. 199-205.
7. Nixon, J. F. Discrete Ice Lens Theory for Frost Heave in Soils. *Canadian Geotechnical Journal*, 1991, 28(6), pp. 843-859.
8. Li, N., Chen, B., Chen, F., and Xu, X. The Coupled Heat-Moisture-Mechanic Model of the Frozen Soil. *Cold Regions Science and Technology*, 2000, 31(3), pp. 199-205.
9. Neaupane, K. M., and Yamabe, T. A Fully Coupled Thermo-Hydro-Mechanical Nonlinear Model for a Frozen Medium. *Computers and Geotechnics*, 2001, 28(8), pp. 613-637.
10. Liu, Z., and Yu, X. Coupled Thermo-Hydro-Mechanical Model for Porous Materials under Frost Action: Theory and Implementation. *Acta Geotechnica*, 2011, 6(2), pp. 51-65.
11. Liu, Z., Sun, Y., and Yu, X. Theoretical Basis for Modeling Porous Geomaterials under Frost Actions: A Review. *Soil Science Society of America Journal*, 2012, 76(2), pp. 313-330.
12. Zhou, M. M., and Meschke, G. A Three-phase Thermo-hydro-mechanical Finite Element Model for Freezing Soils. *International Journal for Numerical and Analytical Methods in Geomechanics*, 2013, 37(18), pp. 3173-3193.
13. Zhang, Y., and Michalowski, R. L. Thermal-Hydro-Mechanical Analysis of Frost Heave and Thaw Settlement. *Journal of Geotechnical and Geoenvironmental Engineering*, 2015, 141(7), 04015027.
14. Rabin, Y., and Steif, P.S. Thermal Stresses in a Freezing Sphere and its Application to Cryobiology. *Journal of Applied Mechanics,* 1998, 65, pp. 328-333.
15. Brownell, D.H., Jr., Garg, S.K., and Pritchett, J.W. Governing Equations for Geothermal Reservoirs. *Water Resources Research,* 1977, 13, pp. 929-934.
16. Kurashige, M. Thermal Stresses of a Fluid-Saturated Poroelastic Hollow Cylinder. *JSME International Journal Series I,* 1992, 35(4), pp. 386-391.
17. Nishimura, S., Gens, A., Olivella, S., and Jardine, R. J. THM-Coupled Finite Element Analysis of Frozen Soil: Formulation and Application. *Géotechnique,* 2009, 59(3), pp. 159-171.
18. Fenton, G. A., and Griffiths, D.V. Bearing Capacity Prediction of Spatially Random c-φ Soils. *Canadian Geotechnical Journal*, 2003, 40(1), pp. 54-65.
19. Griffiths, D.V., Fenton, G. A., and Manoharan, N. Undrained Bearing Capacity of Two-strip Footings on Spatially Random Soil. *International Journal of Geomechanics,* 2006, 6(6), pp. 421-427.
20. Griffiths, D.V., Huang, J., and Fenton, G. A. Probabilistic Infinite Slope Analysis. *Computers and Geotechnics,* 2010, 38(4), pp. 577-584.
21. Bharrucha-Reid, A. T. ed. *Probabilistic Methods in Applied Mathematics*. Academic Press, New York, N.Y, 1968.
22. Sobczyk, K. *Wave propagation in random media.* Elsevier, New York, N.Y, 1985.
23. Chamis, C. C. Probabilistic Structural Analysis Methods for Space Propulsion System Components. *Probabilistic Engineering Mechanics,* 1987, 2(2), pp. 100-110.
24. Fenton, G. A., Griffiths, D. V., and Williams, M. B. Reliability of Traditional Retaining Wall Design. *Geotechique*, 2005, 55(1), pp. 55-62.
25. Andersland, O. B., and Ladanyi, B. *Frozen Ground Engineering*. Wiley, Hoboken, NJ, 2004.

26. Chang, C.S., and Hicher, P.Y. An Elasto-Plastic Model for Granular Materials with Microstructural Consideration. *International Journal of Solids and Structures,* 2005, 42, pp. 4258-4277.
27. Ferber, V., Auriol, J., Magnan, J., Cui, Y., De Laure, E., and Gerente, C. A Microstructural Model for the Volume Changes of Unsaturated Siltey Soils Due to Wetting. *Unsaturated Soils 2006,* pp. 861-872.
28. Helliwell, J. R., Sturrock, C. J., Grayling, K. M., Tracy, S. R., Flavel, R. J., Young, I. M., Whalley, W. R., and Mooney, S. J. Applications of X-ray Computed Tomography for Examining Biophysical Interactions and Structural Development in Soil Systems: a Review. *European Journal of Soil Science,* 2013, 64, pp. 279-297.
29. Tracy, S. R., Daly, K. R., Sturrock, C. J., Crout, N. M. J., Mooney, S. J., and Roose, T. Three-Dimensional Quantification of Soil Hydraulic Properties Using X-ray Computed Tomography and Image-Based Modeling. *Water Resources Research,* 2015, 51(2), pp. 1006-1022.